Lattice Boltzmann algorithm for three-dimensional simulations of plasma turbulence

G. Fogaccia, R. Benzi,* and F. Romanelli
Associazione EURATOM-ENEA sulla Fusione, Centro Ricerche Energia Frascati, Casella Postale 65, 00044 Frascati, Roma, Italy
(Received 4 December 1995)

A lattice Boltzmann algorithm to study the three-dimensional electrostatic-turbulence dynamics in thermonuclear plasmas is derived. The ion continuity, momentum, and pressure equations are reproduced with the electrons being described by the adiabatic response. The numerical stability is discussed. Applications to the study of two-dimensional turbulence are presented. [S1063-651X(96)00709-X]

PACS number(s): 02.70.−c, 52.35.Kt

I. INTRODUCTION

The particle and heat transport across magnetic surfaces in controlled thermonuclear devices is due to turbulent processes associated with the presence of small-scale instabilities, in particular those belonging to the drift branch and destabilized by the free-energy sources related to the presence of density and temperature gradients [1]. Among such instabilities a particular relevance is attributed to the ion temperature gradient (ITG) mode, which is driven unstable by the combined effect of the equilibrium-magnetic-field inhomogeneity and the ion temperature gradient [2–4].

The behavior of the mode in the nonlinear regime has been investigated within the framework of conventional fluid simulations [5–8], gyrokinetic particle simulations [9–11], or gyrofluid simulations [12]. The aim of these analyses has been primarily to determine the magnitude of the turbulent heat flux and its scaling with the plasma parameters both in the case of fixed ion equilibrium temperature profile T_i^{eq} and in the case in which T_i^{eq} is free to evolve. Local flattening of the temperature profile was, e.g., observed in Refs. [5,8] as a result of the turbulent heat flux bringing the mode close to marginal stability. Even though the quasilinear estimate often predicts the correct order of magnitude of the turbulent heat flux, a significant departure from such an estimate has been observed in many cases. For example, in Ref. [8], the formation of large-scale coherent structures was observed, leading to the reduction of the turbulent transport.

Most of the above simulations are two dimensional (2D) and refer to model 1D equilibria such as a plasma slab or a cylinder with circular cross section, where the effect of linear toroidal coupling among different poloidal harmonics is absent. In such a case turbulence is almost isotropic in the plane perpendicular to the equilibrium magnetic field. More recently, attention has been focused on the problem of the formation and evolution of strongly anisotropic structures that have been observed in gyrokinetic particle simulations [10]. Anisotropic turbulence has also been measured [13] on the Tokamak Fusion Test Reactor tokamak [14]. In 2D equilibria, such as those characterizing tokamak plasmas, it can indeed be shown, on the basis of linear theory [15,16], that strongly anisotropic vortices may be generated, with a radial extension of the order of the characteristic length of the equilibrium ion temperature profile $L_T \equiv -(d \ln T_i^{\mathrm{eq}}/dr)^{-1}$ and much larger than the extension in the poloidal direction, which, for the most unstable modes, is of the order of a few ion Larmor radii $\rho_i \equiv v_{\mathrm{th}i}/\Omega_i$, with $v_{\mathrm{th}i}$ being the ion thermal velocity and Ω_i the ion Larmor frequency. The presence of such structures may have a strong impact on the understanding of turbulent transport. The global energy confinement time is indeed expected to increase more weakly with the device dimension than in the case of short radial correlation length turbulence. In order to describe in a realistic way such a situation, 3D simulations are required that should resolve radial wavelengths ranging from the macroscopic device dimension ($\approx L_T$) to the shortest wavelengths at which dissipation takes place, which, for realistic plasma parameters, will be a fraction of the ion Larmor radius, with the wavelengths of the linearly unstable modes being of the order of a few Larmor radii.

In order to perform high-resolution 3D simulations, a particularly promising method is that based on the lattice Boltzmann equation (LBE) [17,18]. The macroscopic dynamics, described by a set of fluid equations, is simulated starting from the microscopic description of the system. To this aim, a population of particles moving on a discrete lattice is considered. Particles that arrive at the same point undergo a collision, with the collision operator chosen in such a way as to conserve the particle number and the momentum. The key issue in the derivation of the LBE algorithm is the choice of the form of the equilibrium distribution function. It is written as a combination of the low-order fluid moments (density, momentum, and pressure) such that the fluid equations on the macroscopic scales (i.e., on a space scale larger than the lattice spacing and a time scale longer than the time between two collisions) are exactly recovered. It is important to note that the microscopic dynamics is, in principle, not related to the true microscopic particle dynamics and, in this respect, the present approach differs from that employed in gyrokinetic simulations [9–11], which solve the exact equation of motion of the particles. However, in many situations, the turbulence dynamics is adequately described by the macroscopic plasma behavior. This is, e.g., the case of the ITG mode well above the linear threshold for instability: in such a case the details of mode-particle resonance, which are im-

*Also at Dipartimento di Fisica Università ''Tor Vergata'' and Instituto Nazionale di Fisica Nucleare, Sezione di Roma II, via E. Carnevale, I-00173, Roma, Italy.

portant in determining the threshold, play a minor role. Under such a condition it may be convenient to employ the LBE approach, which has the advantage of an easy implementation on massively parallel computers. The algorithm has been indeed successfully used for simulations of the Rayleigh-Bénard convection [19] on the APE100 computer [20], as well as to a plasma-physics model, such as the magnetohydrodynamics model [21].

The primary aim of the present paper is to show that a LBE algorithm can be derived for the study of 3D plasma dynamics in the electrostatic limit and within the fluid approximation. The numerical stability of the algorithm is investigated showing that, for an appropriate choice of the parameters, the algorithm is numerically stable. Preliminary applications to the study of 2D turbulence will be also presented.

The structure of the paper is the following. In Sec. II the physical model describing the ITG mode is briefly reviewed and the linear stability is discussed. In Sec. III the lattice Boltzmann method is introduced and the three-dimensional algorithm for the magnetized plasmas is derived. The numerical stability is discussed in Sec. IV. The numerical results are presented in Sec. V and compared with the analytical results of the linear stability analysis. Concluding remarks are given in Sec. VI.

II. TWO-FLUID PLASMA MODEL

In this section the fluid equations describing the ITG mode are briefly described. We refer to Refs. [4,8] for a complete discussion of the model. The basic equations are the continuity, momentum, and pressure equations for the ions,

$$\frac{dn_i}{dt}+n_i\boldsymbol{\nabla}\cdot\mathbf{v}_i=0, \tag{1}$$

$$m_i n_i\frac{d\mathbf{v}_i}{dt}=-\boldsymbol{\nabla}p_i+en_i(-\boldsymbol{\nabla}\phi+\mathbf{v}_i\times\mathbf{B})-\boldsymbol{\nabla}\cdot\boldsymbol{\Pi}_i, \tag{2}$$

$$\frac{dp_i}{dt}=\chi_i\nabla^2 p_i. \tag{3}$$

Here the subscript i refers to the ions; $d/dt=\partial/\partial t+\mathbf{v}_i\cdot\boldsymbol{\nabla}$; m_i, n_i, and $\mathbf{v}_i$ are, respectively, the mass, density, and mean velocity; ϕ is the electrostatic potential, $\mathbf{B}$ is the equilibrium magnetic field, and χ_i the classical thermal conductivity. The expression for the ion stress tensor is given by [22]

$$\boldsymbol{\Pi}_i=-\frac{p_i}{\Omega_i}[2\mathbf{b}(\mathbf{b}\cdot\boldsymbol{\nabla})(\mathbf{v}_{i\perp}\times\mathbf{b})-2(\mathbf{b}\times\boldsymbol{\nabla})v_{i\parallel}\mathbf{b}-(\boldsymbol{\nabla}\times\mathbf{v}_i)\mathbf{b}+\mathbf{b}(\boldsymbol{\nabla}\times\mathbf{v}_i)]-\frac{p_i}{2\Omega_i}[\boldsymbol{\nabla}_\perp(\mathbf{v}_{i\perp}\times\mathbf{b})+(\mathbf{b}\times\boldsymbol{\nabla}_\perp)\mathbf{v}_{i\perp}]-\frac{3}{10}\nu_{ii}\frac{p_i}{\Omega_i^2}\boldsymbol{\nabla}_\perp\mathbf{v}_{i\perp}, \tag{4}$$

where $\mathbf{b}=\mathbf{B}/B$, $\boldsymbol{\nabla}$ is the gradient operator, the suffix $\perp$ ($\parallel$) indicates the component perpendicular (parallel) to the equilibrium magnetic field, and ν_{ii} is the ion-ion collision frequency. Note that the first six terms on the right-hand side correspond to the finite-Larmor-radius effect ($\boldsymbol{\Pi}_{\mathrm{FLR}}$) and should be retained since they cancel part of the contribution associated with the inertia term [23], while the last term corresponds to the effect of perpendicular viscosity dissipation. Equation (3) differs from the pressure equation used in Ref. [8] by small corrections associated with the compressibility term that do not alter the instability dynamics in both the linear and the nonlinear phase.

The electrostatic potential ϕ is determined by the Poisson equation, which, in the limit $k_\perp\lambda_D\ll 1$, with $k_\perp$ being the perpendicular wave vector of the perturbed electrostatic potential and λ_D the Debye length, reduces to the quasineutrality equation

$$n_i=n_e. \tag{5}$$

The electron density is assumed to be described by the adiabatic response

$$n_e=n_e^{\mathrm{eq}}\left(1+\frac{e\phi}{T_e^{\mathrm{eq}}}\right), \tag{6}$$

where T_c^{eq} and n_e^{eq} are the equilibrium electron temperature and density, respectively. This assumption is correct as long as the trapped electron response is small.

Equations (1)–(6) are the usual two-fluid plasma equations employed to analyze the dynamics of ITG modes in three dimensions. In the present paper we will discuss the numerical implementation of the algorithm in the 2D limit. Such a case has been studied in Ref. [8] and it is worthwhile recalling the main results of the linear stability analysis.

In the 2D limit the parallel ion dynamics is neglected by choosing a perturbation with $\mathbf{b}\cdot\boldsymbol{\nabla}=0$. Thus, from Eq. (2), $v_{i\parallel}=0$ and the fluid motion occurs in a plane perpendicular to the equilibrium magnetic field.

As shown in Refs. [4,8], in the low-frequency limit, Eqs. (1) and (3) reduce to

$$\partial_t\hat{\phi}-2\epsilon_T\partial_y\hat{\phi}-2\frac{\epsilon_T}{\tau}\partial_y\hat{p}-\partial_t\nabla^2\hat{\phi},$$

$$-\left[\hat{\phi}+\frac{\hat{p}}{\tau},\nabla^2\hat{\phi}\right]-\frac{1}{\tau}[\partial_x\hat{p},\partial_x\hat{\phi}]-\frac{1}{\tau}[\partial_y\hat{p},\partial_y\hat{\phi}]=-\frac{(D_1-D_2)}{\tau}\nabla^4\hat{p}-D_1\nabla^4\hat{\phi}, \tag{7}$$

$$\partial_t\hat{p}+[\hat{\phi},\hat{p}]=D_2\nabla^2\hat{p}, \tag{8}$$

where $\hat{\phi}=(e\phi/T_e^{\mathrm{eq}})(L_T/\rho_s)$, $\hat{p}=(p_i/p_i^{\mathrm{eq}})(L_T/\rho_s)$, $L_T\equiv-(d\ln T_i^{\mathrm{eq}}/dr)^{-1}$, and $\rho_s\equiv\rho_i\tau^{1/2}$ with $\tau\equiv T_e^{\mathrm{eq}}/T_i^{\mathrm{eq}}$. In order to reproduce the typical situation of the toroidal geometry within the framework of a two-dimensional case, an equilibrium magnetic field $\mathbf{B}=B\mathbf{b}$ with a constant direction $\mathbf{b}$ and a modulus $B=B(x)$, such that $\boldsymbol{\nabla}\times(\mathbf{B}/B^2)=-2/(BR)\hat{\mathbf{y}}$, has been considered, with R being the major radius of the torus. In Eqs. (7) and (8) the time and space variables are normalized respectively to L_T/C_s and to ρ_s, $\epsilon_T\equiv L_T/R$, $[f,g]\equiv\partial_x f\partial_y g-\partial_y f\partial_x g$, $D_1=3\nu_{ii}L_T/10C_s$, $D_2=\chi_i L_T/C_s\rho_s^2$, and $C_s\equiv v_{\mathrm{th}i}\tau^{1/2}$.

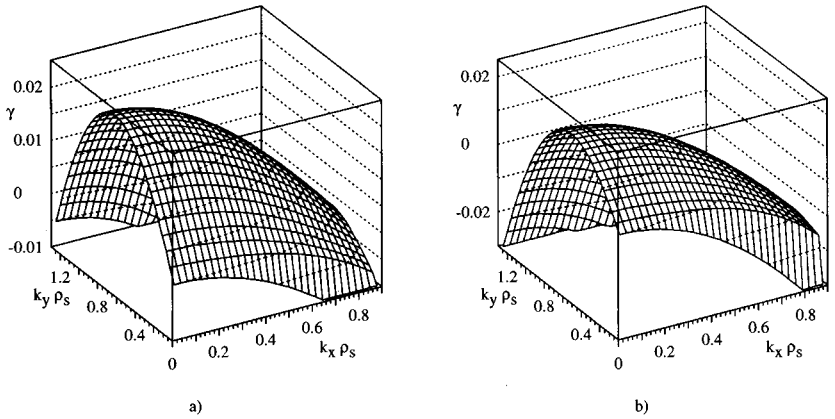

FIG. 1. Linear growth rate normalized to the ratio L_T/C_s versus $(k_x\rho_s, k_y\rho_s)$, where $L_T=-(d \ln T_i/dr)^{-1}$, $C_s=v_{\mathrm{thi}}\tau^{1/2}$, $\tau=T_e^{\mathrm{eq}}/T_i^{\mathrm{eq}}$, and $\rho_s=\rho_i\tau^{1/2}$. k_x and k_y are the components of the wave vector, perpendicular to the equilibrium magnetic field. Also shown are the result of Eq. (9) for $\tau=12$, $\epsilon_T=0.025$, and two different values of the classical dissipation: (a) $D_1=D_2=0.023$, and (b) $D_1=D_2=0.046$.

In Eq. (7) the first term comes from the temporal partial derivative of the perturbed ion density. The next two terms are the contributions to $\nabla\cdot n_i\mathbf{v}_i$ coming from the $\mathbf{E}\times\mathbf{B}$ drift and the diamagnetic drift, respectively, and they are associated with the inhomogeneity of the equilibrium magnetic field. The terms including the D_1 coefficient are related to the viscosity, while the remaining contributions are related to the polarization drift. Upon linearizing and Fourier transforming ($\partial_t=-i\omega$, $\nabla=i\mathbf{k}_\perp$) Eqs. (7) and (8), the following dispersion relation is obtained:

$$(1+k_\perp^2)\omega^2+\left\{\left(\frac{k_\perp^2}{\tau}+2\epsilon_T\right)k_y+i[D_1k_\perp^4+D_2k_\perp^2(1+k_\perp^2)]\right\}\omega+\left[\frac{2\epsilon_T}{\tau}k_y^2-D_1D_2k_\perp^6+ik_yk_\perp^2\left(2\epsilon_TD_2+D_1\frac{k_\perp^2}{\tau}\right)\right]=0. \tag{9}$$

The growth rate γ obtained by solving Eq. (9) is shown in Fig. 1 vs $(k_x\rho_s, k_y\rho_s)$ for $\tau=12$, $\epsilon_T=0.025$, and two values of the classical dissipation $D_1=D_2=+0.023$ [Fig. 1(a)] and $D_1=D_2=0.046$ [Fig. 1(b)]. It is important to stress that classical dissipation weakly affects the most unstable long-wavelength modes. Equation (9) yields also a threshold in ϵ_T for the mode destabilization, given, for $k_\perp=0$, by $0\leqslant\epsilon_T\leqslant 2/\tau$.

III. LATTICE BOLTZMANN EQUATION FOR MAGNETIZED PLASMAS

The lattice Boltzmann equation [17] is a numerical technique that has been used to integrate the Navier-Stokes equation [18,19]. The macroscopic dynamics is simulated by a fictitious microscopic system of particles moving on a discrete D-dimensional lattice, as schematically shown in Fig. 2 for the case $D=2$. The elementary process corresponds to the particle propagation between each site and one of the b neighboring sites (which depends on the orientation of the particle velocity), and the collision between particles that arrive at the same time in a given site. The collision operator must satisfy the conditions of particle-number and momentum conservation. Under the effect of collisions, the system relaxes toward a local equilibrium distribution function. The choice of the equilibrium distribution function is the crucial point in the derivation of the LBE algorithm. It is written as a combination of the low-order fluid moments chosen in such a way that the macroscopic dynamics, described by the fluid equations, is correctly reproduced. The lattice dimension D is chosen in order to ensure the isotropy of the macroscopic system simulated by the LBE.

In the case of 3D simulations, considered in the present section, a face-centered-hypercubic (FCHC) four-dimensional lattice must be used. Each quantity is assumed to depend only on the first three coordinates, associated with the three spatial variables, and to be constant along the fourth (unphysical) direction. On each site, $b=24$ populations of particles $\{N_i, i=1,2,\ldots,b\}$ are defined with velocities $\{c_{i\alpha}, i=1,2,\ldots,b: \alpha=1,\ldots,D\}$. In the following, the Greek subscripts represent the components of a four-dimensional vector, while the usual notation $\mathbf{v}$ represents a three-dimensional vector. As it will be shown below, in order to reproduce the two-fluid model the N_i populations must

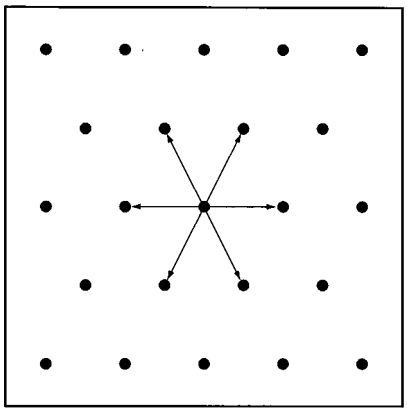

FIG. 2. Discrete two-dimensional lattice. On each site, $b=6$ populations of particles $\{N_i, i=1,\ldots,6\}$ are defined with velocities $\{\mathbf{c}_i, i=1,\ldots,6\}$, joining the site with the six neighboring sites.

evolve in time according to propagation and collision rules, which can be written as

$$N_i(\mathbf{r}+\Delta r\mathbf{c}_i,t+\Delta t)=N_i(\mathbf{r},t)+\nu_c\Delta t\sum_{j=1}^{b}A_{ij}[N_j(\mathbf{r},t)-N_j^{\mathrm{eq}}(\mathbf{r},t)]+B_0\sum_{j=1}^{b}B_{ij}N_j(\mathbf{r},t), \tag{10}$$

$\mathbf{r}$ being the coordinate of the site, $\Delta r|\mathbf{c}_i|$ and Δt the microscopic steps, physically related to the mean free path and to the time between two collisions, respectively, with $\Delta r=(2T_e^{\mathrm{eq}}/m_i)^{1/2}\Delta t$, ν_c being the collision frequency, A_{ij} the collision matrix, N_j^{eq} the value of the population N_j at the local thermodynamic equilibrium, and $B_0=\Omega_i\Delta t$ with $\Omega_i=\Omega_i(x)=eB(x)/m_i$.

The collision matrix A_{ij} must satisfy the mass and momentum conservation laws and appropriate symmetries [17] and has the same expression previously employed for simulating the Navier-Stokes equation. It is possible to show [24] that A_{ij} can be written in terms of just one parameter λ, connected to the kinematic viscosity ν by

$$\nu=-\frac{1}{3\lambda}-\frac{1}{6}. \tag{11}$$

The matrix A_{ij} is evaluated in Ref. [24].

The matrix B_{ij}, which accounts for the Lorentz force, has the following explicit expression in terms of the equilibrium magnetic field vector $\mathbf{b}$:

$$B_{ij}=\tfrac{1}{12}\mathbf{b}\cdot\mathbf{c}_i\times\mathbf{c}_j. \tag{12}$$

Note that in the numerical evolution of the LBE the temporal variable will be normalized to Δt and the spatial variable to Δr (lattice units), but, in order to discuss the fluid-equations derivation, it is convenient to maintain explicit the dependence on Δr and Δt.

In order to explicitly show that Eq. (10) correctly reproduces the two-fluid model, it is necessary to derive the associated macroscopic equations by the usual multiscale expansion of the LBE [17] similar to the well known Chapman-Enskog [25] expansion of the kinetic equation. It is important to note that in the LBE formalism, the collision time (ν_c^{-1}) and the discrete time step (Δt) are assumed to be equal (i.e., $\nu_c\Delta t=1$). Thus the continuous limit ($\Delta t\to 0$) and the multiscale expansion, made in order to derive the macroscopic equations, are taken simultaneously. The expansion parameter (ϵ) is the ratio between the microscopic time scale ν_c^{-1} and the time scale of the macroscopic variables. Space and time derivatives are ordered in terms of ϵ as

$$\nabla=O(\epsilon)\Delta r^{-1},\quad \partial_t=O(\epsilon)\Delta t^{-1}. \tag{13}$$

Furthermore, we assume $\Omega_i\Delta t=O(\epsilon)$. Formally, the effect of viscosity enters at $O(\epsilon^2)$ for perturbations characterized by the typical length scale $\epsilon^{-1}\Delta r$. Nevertheless, for perturbations on smaller scale $\epsilon^{-1/2}\Delta r$, the viscosity term enters at $O(\epsilon)$ and, properly, provides an energy sink for the high wave numbers.

Generally, the local equilibrium population is a function of the macroscopic variables. The mass density ρ, the momentum density $\mathbf{J}$, and the thermal pressure p can be expressed, in lattice units, in terms of linear combinations of the microscopic variables N_i (the normalization $m_i=1$ is considered in the following for the sake of simplicity):

$$\rho=\sum_{i=1}^{24}N_i,\quad \mathbf{J}=\sum_{i=1}^{24}\mathbf{c}_iN_i,\quad p\equiv J_4=\sum_{i=1}^{24}c_{i4}N_i.$$

In order to reproduce the fluid equations, the expression of N_i^{eq} must be chosen as

$$N_i^{\mathrm{eq}}=\tfrac{1}{24}\{\rho+2J_\alpha c_{i\alpha}+3[Q_{i\alpha\beta}J_\alpha v_\beta-Q_{i44}J_\gamma v_\gamma]-12pQ_{i44}\}+\tfrac{1}{8}Q_{i\alpha\beta}\hat{\Pi}_{\alpha\beta}, \tag{14}$$

where the repeated indices are summed, $v_\alpha=J_\alpha/\rho$, $Q_{i\alpha\beta}=c_{i\alpha}c_{i\beta}-\frac{1}{2}\delta_{\alpha\beta}$, and $\hat{\mathbf{\Pi}}$ is the $\mathbf{\Pi}_{\mathrm{FLR}}$ tensor expressed in lattice units.

In order to obtain the expression of the physical variables, the following scale transformation must be performed:

$$\rho\to\rho\,\frac{m_i}{(\Delta r)^3},\quad \mathbf{v}\to\mathbf{v}\,\frac{\Delta r}{\Delta t}, \tag{15}$$

$$\mathbf{J}\to\mathbf{J}\,\frac{m_i}{\Delta t(\Delta r)^2},\quad p\to 2p\,\frac{T_e^{\mathrm{eq}}}{(\Delta r)^3}, \tag{16}$$

$$\nu\to\nu\,\frac{(\Delta r)^2}{\Delta t},\quad \hat{\Pi}\to\hat{\Pi}\,\frac{m_i}{\Delta r(\Delta t)^2}. \tag{17}$$

With such a choice, the physical variables satisfy the equations

$$\frac{\partial\rho}{\partial t}+\nabla\cdot\mathbf{J}=0, \tag{18}$$

$$\frac{\partial\mathbf{J}}{\partial t}+[(\mathbf{v}\cdot\nabla)\mathbf{J}+\mathbf{J}(\nabla\cdot\mathbf{v})]=-\frac{T_e^{\mathrm{eq}}}{m_i}\nabla\rho-\nabla p+\frac{e}{m_i}\mathbf{J}\times\mathbf{B}+\nu[\nabla^2\mathbf{J}+\tfrac{1}{2}\nabla(\nabla\cdot\mathbf{J})]-\nabla\cdot\mathbf{\Pi}_{\mathrm{FLR}}, \tag{19}$$

$$\frac{\partial p}{\partial t}+[(\mathbf{v}\cdot\nabla)p+p(\nabla\cdot\mathbf{v})]=\nu\nabla^2p. \tag{20}$$

Equations (18)–(20) coincide with Eqs. (1)–(3), except for the compressibility term in the pressure equation. The effect of such a term is negligible as long as $\tau\gg 1$.

Lattice Boltzmann equation in the 2D limit

The lattice Boltzmann algorithm described so far is able to simulate the 3D ITG mode dynamics. In the present paper we will consider the application to the 2D limit. To this aim, it is convenient to consider the reduction of the lattice Boltzmann algorithm to the two-dimensional dynamics.

In order to reproduce the macroscopic equations (18)–(20) in two dimensions for the mass density, the momentum density, and the pressure field, it is convenient to consider

the three-dimensional lattice obtained by the projection of the FCHC lattice on the hyperplane (x,y,z) (the so-called pseudo-four-dimensional model).

The original 24 vectors ($b=24$) of the 4D lattice can be distinguished, according to their components along the fourth dimension, into two groups: a first group of 12 four-dimensional vectors orthogonal to the fourth direction and a second group of six pairs of vectors, with the vectors of each pair differing for the sign of the fourth component [e.g., (c_x,c_y,c_z+1) and $(c_x,c_y,c_z,-1)$]. By projecting on the 3D lattice, each of the six pairs is projected on the same vector and the number of distinct links becomes 18. The corresponding particle populations N_i,N_j, which differ in the fourth component of the velocity in the FCHC model, are degenerate in the three-dimensional lattice. Thus, in the pseudo-four-dimensional model, it is necessary to introduce different weights s_i for each propagation direction $\mathbf{c}_i$: $s_i=1$ for the link $\mathbf{c}_i$ that at most one particle population can propagate along, corresponding to the vectors of the first group, and $s_i=2$ for the link $\mathbf{c}_i$ that two particle populations can propagate along, corresponding to the vectors of the second group.

The macroscopic variables become

$$\rho=\sum_{i=1}^{18} s_i N_i, \quad \mathbf{J}=\sum_{i=1}^{18} s_i \mathbf{c}_i N_i,$$

Note that, if the pseudo-four-dimensional lattice is employed to simulate the 2D dynamics, the J_4 field is annihilated and the thermal pressure can be identified with the J_3 field. Taking the magnetic field along the z axis, the B_{ij} matrix becomes

$$B_{ij}=\frac{s_j}{12}(c_{ix}c_{jy}-c_{iy}c_{jx}) \tag{21}$$

and the $\mathbf{J}\times\mathbf{B}$ force acts on the (x,y) plane.

IV. NUMERICAL STABILITY

In the present section, the numerical stability of the LBE will be discussed in the 2D limit. Since the parallel dynamics is not affected by the presence of the equilibrium magnetic field, the numerical stability of the 3D system can be discussed in a similar way.

The numerical stability can be conveniently discussed by considering separately long- and short-wavelength modes. In order to identify the terms responsible for the numerical instability at long wavelength it is convenient to consider the macroscopic equations that are obtained by expanding the LBE to second order in ϵ, yielding

$$\frac{\partial\rho}{\partial t}+\nabla\cdot\mathbf{J}+\frac{\Delta t}{2}\nabla\cdot\left(\frac{e}{m_i}\mathbf{J}\times\mathbf{B}\right)=0, \tag{22}$$

$$\frac{\partial\mathbf{J}}{\partial t}+[(\mathbf{v}\cdot\nabla)\mathbf{J}+\mathbf{J}(\nabla\cdot\mathbf{v})]=-\frac{T_e^{\mathrm{eq}}}{m_i}\nabla\rho-\nabla p+\frac{e}{m_i}\mathbf{J}\times\mathbf{B}+\nu[\nabla^2\mathbf{J}+\tfrac{1}{2}\nabla(\nabla\cdot\mathbf{J})]-\nabla\cdot\mathbf{\Pi}_{\mathrm{FLR}}-\frac{\Delta t}{2}\frac{\partial}{\partial t}\left(\frac{e}{m_i}\mathbf{J}\times\mathbf{B}\right), \tag{23}$$

$$\frac{\partial p}{\partial t}+[(\mathbf{v}\cdot\nabla)p+p(\nabla\cdot\mathbf{v})]=\nu\nabla^2 p. \tag{24}$$

It is important to stress that Eqs. (22)–(24) are valid only for long-wavelength modes ($k\Delta r\ll 1$). From the above system it is possible to see that a term associated with the magnetic field appears in the continuity and momentum equations, whereas the usual dissipative terms appear in the momentum and pressure equations. The term that appears in the momentum equation introduces an effect of order $\omega\Delta t\ll 1$ with respect to the destabilizing term present in the continuity equation and therefore its effect is negligible. The linear stability of the corresponding system of equations can be performed as shown in Sec. II, yielding an unphysical instability, whose growth rate γ^{num} is given, in the absence of a pressure gradient, by

$$\gamma^{\mathrm{num}}\approx\frac{\Omega_i^2\Delta t}{2}\frac{\tau k_\perp^2\rho_i^2}{1+\tau k_\perp^2\rho_i^2}, \tag{25}$$

and, in the presence of a pressure gradient, but below the ITG threshold, by

$$\gamma^{\mathrm{num}}\approx\frac{\Omega_i^2\Delta t}{2}. \tag{26}$$

Thus the growth rate increases as the square of the magnetic field strength. As the typical wave numbers of the unphysical instability are small, the mode energy is weakly dissipated by viscosity. Thus such an unphysical instability may be particularly dangerous in the presence of an inverse energy cascade. In order to annihilate the effect of the unphysical destabilizing terms $O(\epsilon^2)$, without modifying the macroscopic equation, an *ad hoc* corrective term has been added to the right-hand side of Eq. (10):

$$-\frac{B_0^2}{24}\sum_{j=1}^{18} s_j(c_{ix}c_{jx}+c_{iy}c_{jy})N_j(\mathbf{r},t). \tag{27}$$

The expression of the corrective term in three dimensions is

$$-\frac{B_0^2}{24}\sum_{j=1}^{24}(\mathbf{c}_i\cdot\mathbf{c}_j-\mathbf{b}\cdot\mathbf{c}_i\mathbf{b}\cdot\mathbf{c}_j)N_j(\mathbf{r},t). \tag{28}$$

It is straightforward to verify that the additional term in B_0^2 has no effect on the continuity equation and on the pressure evolution equation. It only produces, in the momentum equation (23), a damping term of the form $-\Omega_i^2\Delta t\mathbf{J}/2$, which cancels exactly, in the linear dispersion relation, the unphysical destabilizing contribution coming from terms of $O(\epsilon^2)$.

In the case of arbitrary wavelengths, the stability of the system must be investigated numerically by linearizing Eq. (10) around an equilibrium configuration and taking

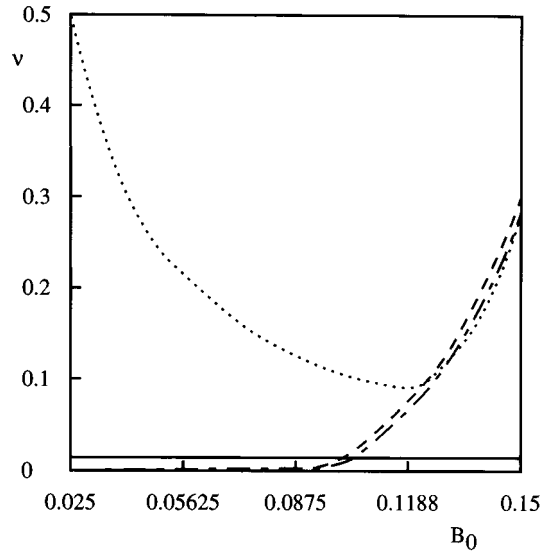

FIG. 3. Threshold of viscosity (in lattice units) vs $B_0=\Omega_i\Delta t$. In the region below the curves, the lattice Boltzmann algorithm develops numerical instabilities. The continuous line is the viscosity threshold in the Navier-Stokes case; the dashed line is the result in the presence of the magnetic field, but neglecting the finite-Larmor-radius effect; the dotted line takes into account the finite-Larmor-radius term; finally, the dash-dotted line is the result obtained by a smoothing technique, used in order to eliminate the numerical instabilities at short wavelengths, coming from the FLR term. The LBE has been linearized around a homogeneous equilibrium configuration with $L=512$, $p_0=1$, and $\rho_0=24$.

$N_j(\mathbf{r},t)\propto e^{\gamma t+i\mathbf{k}\cdot\mathbf{r}}$. In the present case, the stability will depend both on ν and B_0. The results of the numerical analysis are shown in Fig. 3, where the region in (B_0,ν) space with no unstable modes is displayed. The system is numerically stable above the various curves. Equation (10) has been linearized around the following homogeneous equilibrium configuration

$$\rho_{\rm eq}=\rho_0, \quad p_{\rm eq}=p_0, \quad \mathbf{J}_{\rm eq}=\mathbf{0}, \quad \boldsymbol{\nabla}B=\mathbf{0},$$

with $p_0=1$ and a square lattice $L\times L$ with $L=512$. The continuous line is the result obtained in the Navier-Stokes case ($B_0=0$). As shown in Ref. [17], when viscosity becomes too small $\nu<0.013$, modes with wavelength comparable to the lattice constant are excited and numerical instabilities develop. The dashed line is the numerical result obtained in the presence of the magnetic field, but neglecting the finite Larmor radius effect ($\hat{\Pi}_{\alpha\beta}=0$). For $B_0\leqslant 0.1$, the viscosity threshold is the same as in the $B_0=0$ case. Indeed, the numerical instabilities driven by the magnetic field, at long wavelengths, have been annihilated by the corrective term Eq. (27). As B_0 approaches unity, the expression Eq. (27), obtained in the limit $B_0\ll 1$, is not appropriate to eliminate numerical instabilities and the viscosity threshold increases. When the finite Larmor radius term $\hat{\Pi}_{\alpha\beta}$ is taken into account (dotted line), numerical instabilities at short wavelengths ($k_\perp\rho_i>1$) appear and the viscosity threshold becomes about one order of magnitude larger than in the case without the magnetic field. Note that the viscosity threshold becomes larger as B_0 decreases since $\hat{\Pi}_{\alpha\beta}\propto B_0^{-1}$. However, the dynamics of electrostatic turbulence is not correctly described in the limit $k_\perp\rho_i>1$ by the fluid approximation. Thus it is convenient to eliminate the term $\hat{\Pi}_{\alpha\beta}$ in such a wavelength range. In the present case this is obtained by performing a smoothing of the velocity fields, used to evaluate $\hat{\Pi}_{\alpha\beta}$, over a radial extent of order ρ_i. The dash-dotted line is the result obtained by a smoothing technique, which uses, at each site, $N=25$ neighboring sites in order to smooth the velocity fields. Note that the $\hat{\Pi}_{\alpha\beta}$ term is fully included for $k_\perp\rho_i<1$.

In order to reproduce the effect of energy sources present in tokamak plasmas, the macroscopic equilibrium configuration must not decay over the dissipative time scale. Thus sources of momentum and pressure must be included.

In the numerical simulations, in order to investigate the linear phase of the ITG modes, the system has been perturbed around the equilibrium solution obtained in the drift approximation

$$\rho_{\rm eq}=\rho_0, \quad p_{\rm eq}=p_{\rm eq}(x), \quad \mathbf{J}_{\rm eq}=\mathbf{J}_d, \tag{29}$$

where $\mathbf{J}_d=(0,p'_{\rm eq}/B_0)$ is the diamagnetic density current. In this case, the momentum source (in lattice units) $\mathbf{S}_J$ must be taken in a such way as to balance the damping of the equilibrium current density, coming from the viscosity term, and the finite-Larmor-radius term

$$\mathbf{S}_J=-\nu\nabla^2\mathbf{J}_{\rm eq}+\boldsymbol{\nabla}\cdot\hat{\Pi}^{\rm eq}. \tag{30}$$

Similarly, the damping effect on the equilibrium pressure will be canceled by a source of the form (in lattice units)

$$S_p=-\nu\nabla^2 p_{\rm eq}. \tag{31}$$

In addition to the previous terms, sources that balance the $O(\epsilon^2)$ terms in the macroscopic equations are necessary. Thus an additional source for the equilibrium current density must be introduced, of the form (in lattice units)

$$\mathbf{S}_J^{(1)}=\tfrac{1}{2}B_0^2\mathbf{J}_{\rm eq}, \tag{32}$$

which balances, in the momentum equation, the unphysical damping related to the corrective term (27). For the same reason, a term of the form

$$S_\rho=\tfrac{1}{2}\boldsymbol{\nabla}\cdot(\mathbf{J}_{\rm eq}\times B_0\mathbf{b}+\mathbf{S}_J) \tag{33}$$

must be introduced in the continuity equation. The addition of the source terms in the macroscopic equations yields the following equations for the populations:

$$N_i(\mathbf{r}+\mathbf{c}_i,t+1)=N_i(\mathbf{r},t)+\sum_{j=1}^{18}A_{ij}[N_j(\mathbf{r},t)-N_j^{\rm eq}(\mathbf{r},t)]$$
$$+B_0\sum_{j=1}^{18}B_{ij}N_j(\mathbf{r},t)-\frac{B_0^2}{24}$$
$$\times\sum_{j=1}^{18}s_j(c_{ix}c_{jx}+c_{iy}c_{jy})N_j(\mathbf{r},t)+\tfrac{1}{12}\mathbf{c}_i\cdot(\mathbf{S}_J$$

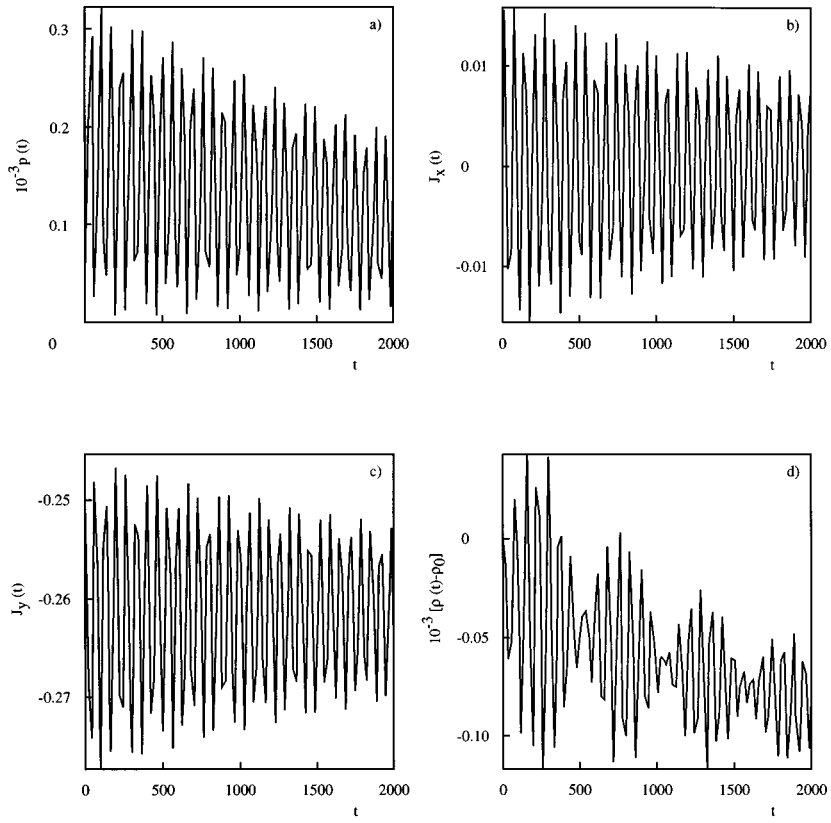

FIG. 4. Equilibrium macroscopic variables vs t (in lattice units), at the point ($x=L/4$, $y=L/4$), obtained by a LBE simulation with $L=512$, $p_{\rm eq}=p_0\sin(4\pi x/L)$, $p_0=1$, $B_0=0.1$, $\rho_0=24$, and $\nu=0.02$. The macroscopic variables are the pressure p (a), the x,y components of the momentum density J_x, J_y, respectively (bc), and the density fluctuation $\tilde{\rho}=\rho-\rho_0$ (d).

$$+\mathbf{S}_J^{(1)})+\tfrac{1}{12}c_{iz}S_p+\tfrac{1}{24}S_\rho\,. \tag{34}$$

The numerical stability of the above system has been verified by initializing an equilibrium configuration with a homogeneous equilibrium magnetic field. At the starting time the microscopic populations have been set to the thermodynamic equilibrium values $N_i(\mathbf{r},0)=N_i^{\rm eq}(\rho,\mathbf{J},p)$ corresponding to the macroscopic configuration, given by Eq. (29). As the system evolves in time, the macroscopic variables remain constants [the numerical fluctuations are of $O(10^{-2})$ for a square lattice $L\times L$ with $L=512$], as expected for a configuration that is linearly stable (since $\nabla B=0$). The results of the simulation, performed with a pressure profile $p_{\rm eq}=p_0\sin(4\pi x/L)$ and the parameter values $L=512$, $p_0=1$, $B_0=0.1$, and $\rho_0=24$ are shown in Fig. 4. The macroscopic variables p, J_x, J_y, and $\tilde{\rho}\equiv\rho-\rho_0$, in lattice units, are plotted versus time at the lattice point $x=L/4$, $y=L/4$. Thus the numerical algorithm is indeed stable.

V. NUMERICAL RESULTS

After having shown that the LBE algorithm is numerically stable, in this section the linear and the nonlinear evolution are considered. The comparison of the numerical results with the analytical results of Sec. II will provide a test for the accuracy of the method.

The linear phase of the instability has been studied by considering a nonuniform magnetic field of the form $B_0=\hat{B}_0[1+\epsilon_B\cos(2\pi x/L)]$, with the constant ϵ_B being proportional to the magnetic field inhomogeneity. The microscopic populations have been perturbed around the equilibrium values in order to produce a density fluctuation $\tilde{\rho}=\Sigma_{k_x,k_y}[\rho_1\sin(k_xx+k_yy)+\rho_2\cos(k_xx+k_yy)]$ with $k_{x,y}=2\pi n_{x,y}/L$ the wave vectors of the perturbation. In Fig. 5 the linear and turbulent phases are shown for an equilibrium magnetic field with $B_0=0.1$ and $\epsilon_B=0.1$. The macroscopic variables are plotted as functions of the time at $x=L/4$, $y=L/2$ for $L=512$ and for a starting density perturbation characterized by $n_x=0$ and $n_y=3,4,5,6$. The numerical simulation has been performed for $p_0=1$ and for a viscosity value $\nu=0.02$. The linear growth rate (in lattice units) obtained from the local dispersion relation ($\gamma_{\rm lin}$) is plotted versus the spatial x coordinate in Fig. 6 for $L=512$, $n_x=0$, and $n_y=3$. The numerically determined growth rate is also shown (the point at $x=L/4$). An estimate of the global eigenvalue can be obtained by observing that the eigenfunction tends to be localized during the linear phase around $x=L/4$ as shown in Fig. 7. Thus the global growth rate is expected to be close to the linear growth rate evaluated at $x=L/4$, as indeed shown in Fig. 6.

The evolution of the pressure profile, in lattice units, at different y values is shown in Fig. 8. Figures 8(a), 8(b), and 8(c) represent the pressure profile, respectively, at $y=L/4$, $y=L/2$, and $y=3L/4$ for different times: at the starting time (solid line), during the linear phase (dashed line), and during the turbulent phase (dotted line). The pressure profile does not show the local flattening, observed in Refs. [5, 8], since, for the present simulation, the typical diffusion time, associated with the turbulent heat flux, is much longer than the time of the simulation.

The evolution of the turbulent heat flux normalized to $2T_e^{\rm eq}/\Delta t(\Delta r)^2$, $q_x\equiv L^{-1}\int dy\, v_x p_i$, at $x=L/4$ is shown in Fig. 9, where the ratio between q_x and the quasilinear esti-

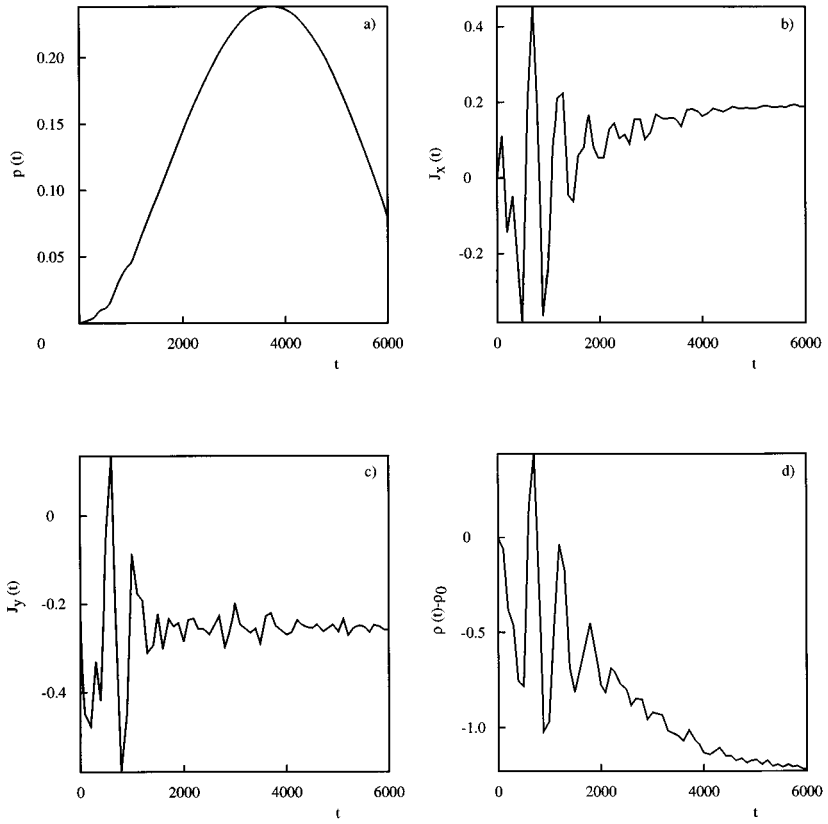

FIG. 5. Temporal behavior of the macroscopic variables, in lattice units, at the point ($x=L/4$, $y=L/4$), in the presence of the ITG mode. A nonuniform magnetic field $B_0=\hat{B}_0[1+\epsilon_B\cos(2\pi x/L)]$ with $\hat{B}_0=0.1$, $\epsilon_B=0.1$, $L=512$, $\nu=0.02$, and a starting density perturbation $\tilde{\rho}=\Sigma_{k_x,k_y}[\rho_1\sin(k_x x+k_y y)+\rho_2\cos(k_x x+k_y y)]$ with wave numbers $n_x=0$, $n_y=3,4,5,6$ have been considered. The figure shows the same quantities as in Fig. 4.

mate is plotted vs time. The quasilinear estimate of the heat flux is derived on the basis of the usual mixing-length argument by assuming a diffusive heat flux $q_x^{\mathrm{qlin}}=\chi_{an}\nabla p_{\mathrm{eq}}$, with $\chi_{an}\approx\gamma/k_x^2$, γ being the linear growth rate and k_x being an estimate of the average wave vector of the perturbation. In the present case, $k_x=12\pi/L$ has been assumed. As shown in Fig. 9, the heat flux increases during the linear phase approaching the quasilinear value at $t=2000$. In the turbulent phase, the heat flux decreases and reaches at saturation a value that is 30% smaller. Such a reduction has been observed also in previous fluid simulations [8] and gyrokinetic particle simulations [9]. In Ref. [8], the phenomenon has been explained in terms of the formation of large-scale coherent structures. These structures can be interpreted as solitary-vortex solutions of the inviscid equations and are

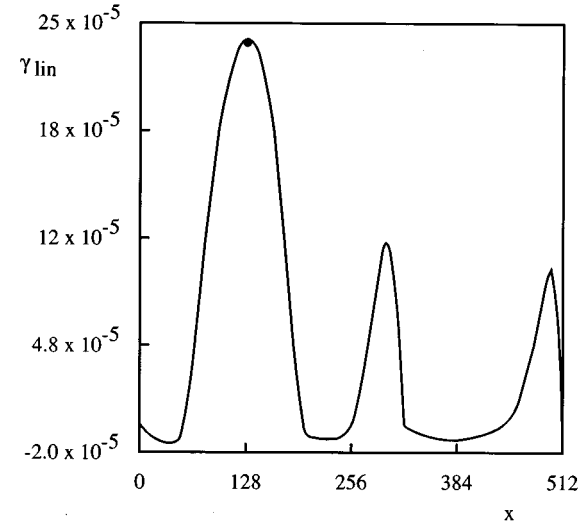

FIG. 6. Linear growth rate vs the x coordinate in lattice units (solid line) for a starting density perturbation with wave numbers $n_x=0$, $n_y=3$. The corresponding value of the numerical growth rate is also shown (point at $x=128$).

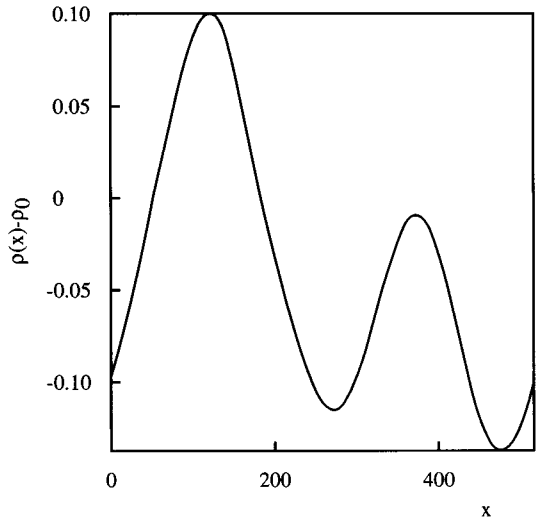

FIG. 7. Linear mode structure at the end of the linear phase. The variables plotted are expressed in lattice units.

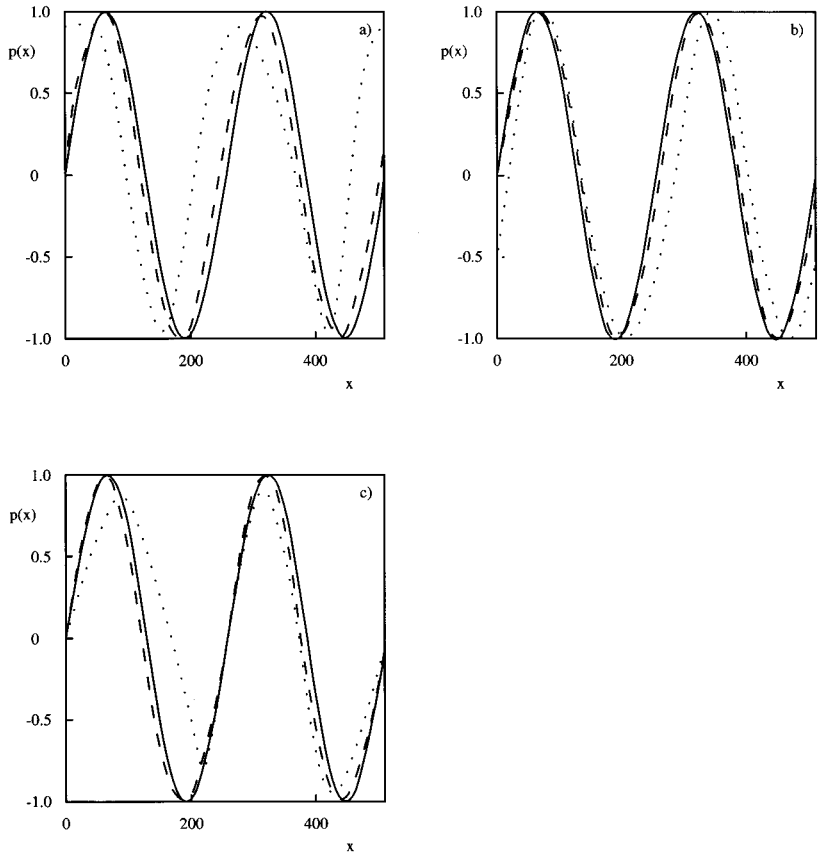

FIG. 8. Evolution of the pressure profile at different y values (in lattice units): (a) $y=L/4$, (b) $y=L/2$, and (c) $y=3L/4$, with $L=512$. The solid line is the pressure profile at the starting time, the dashed line is the pressure during the linear phase ($t=2000$), and the dotted line is the pressure profile during the turbulent phase ($t=6000$).

characterized by a turbulent heat flux that exactly vanishes.

Large-scale structures are also observed in the present simulations as shown in Fig. 10, where the contour plots of pressure and density are shown at $t=6000$. From these results we can conclude that the LBE algorithm correctly reproduces the turbulent dynamics.

VI. CONCLUSION

A lattice Boltzmann algorithm, which simulates the plasma turbulence driven by the ion temperature gradient and by the curvature of the equilibrium magnetic field, has been developed. The algorithm reproduces the ion continuity, momentum, and pressure equations in three dimensions, with the electrons being described by the adiabatic response. The magnetic field term produces long-wavelength numerical instabilities, which can be suppressed by inserting a corrective term that enters the momentum equation at the second order in Δt and so does not alter the form of the fluid equations in the continuous limit $\Delta t \rightarrow 0$. Short-wavelength instabilities, coming from the finite-Larmor-radius term, are suppressed by performing a smoothing of the velocity fields, over a radial extent of order ρ_i. Then, the finite value of the viscosity can be chosen of the same order of the value that is needed to obtain numerically stable Navier-Stokes simulations.

The 2D limit has been analyzed. In the linear phase the growth rate obtained from the lattice Boltzmann simulations

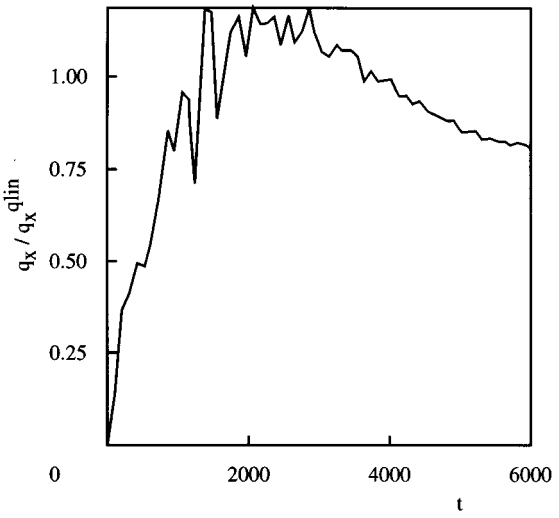

FIG. 9. Ratio between the heat flux $q_x \equiv L^{-1} \int dy\, v_x p_i$ and the quasilinear estimate vs time (in lattice units) at $x=L/4$, with $L=512$. The quasilinear estimate $q_x^{\mathrm{qlin}} = \chi_{an} \nabla p_{\mathrm{eq}}$, with $\chi_{an} \approx \gamma / k_x^2$, γ being the linear growth rate, is evaluated for an equilibrium pressure profile $p_{\mathrm{eq}} = p_0 \sin(4\pi x/L)$, with $p_0=1$, and an average wave vector of the perturbation $k_x = 12\pi/L$.

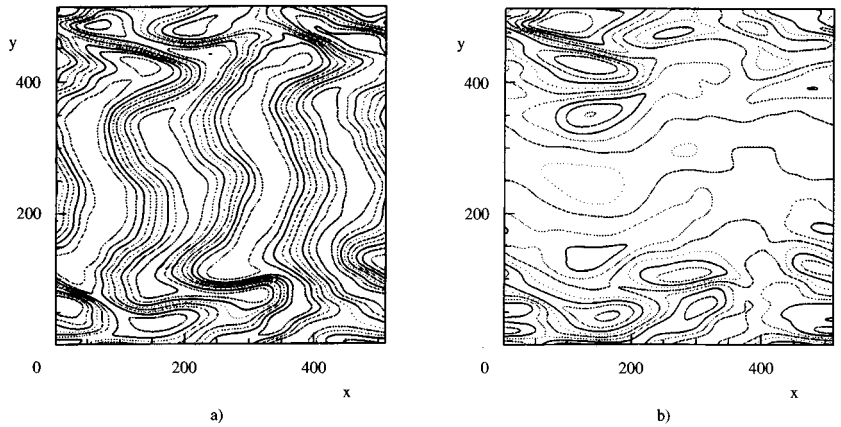

FIG. 10. Contour plots of the (a) pressure and (b) electrostatic potential in lattice units at $t=6000$.

is in agreement with the growth rate obtained from the linear theory. In the nonlinear phase the relaxation towards a marginally stable profile is observed. A complete discussion of the dynamics of the turbulent phase is planned to be presented in a future paper. For a LBE simulation followed up to 6000 time units on a lattice 512×512, the typical CPU time is about 71 h on an IBM RISC/6000 Model No. 370 and the necessary memory region is about 23 Mbytes.

ACKNOWLEDGMENT

We thank F. Massaioli for having supplied us with the original LBE code that simulates the Navier-Stokes equation.

[1] F. Romanelli, Plasma Phys. Controlled Fusion **31**, 1535 (1989).
[2] W. Horton, D. I. Choi, and W. M. Tang, Phys. Fluids **24**, 1077 (1981).
[3] B. Coppi and F. Pegoraro, Nucl. Fusion **17**, 969 (1977).
[4] F. Romanelli, Phys. Fluids B **1**, 1018 (1989).
[5] W. Horton, R. D. Estes, and D. Biskamp, Plasma Phys. **22**, 663 (1980).
[6] B. G. Hong and W. Horton, Phys. Fluids B **2**, 978 (1990).
[7] R. E. Waltz, Phys. Fluids **31**, 1962 (1988).
[8] M. Ottaviani, F. Romanelli, R. Benzi, M. Briscolini, P. Santangelo, and S. Succi, Phys. Fluids B **2**, 67 (1990).
[9] W. W. Lee and W. M. Tang, Phys. Fluids **31**, 612 (1988).
[10] S. E. Parker, W. W. Lee, and R. A. Santoro, Phys. Rev. Lett. **71**, 2042 (1993).
[11] S. Briguglio, G. Betello, G. Fogaccia, S. Graziadei, S. C. Guo, C. Kar, F. Romanelli, G. Vlad, and F. Zonca, in *Plasma Physics and Controlled Nuclear Fusion Research 1992* (International Atomic Energy Agency, Vienna, 1992), Vol. 2, p. 87.
[12] G. W. Hammett, M. A. Beer, W. Dorland, S. C. Cowley, and S. A. Smith, Plasma Phys. Controlled Fusion **35**, 973 (1993).
[13] N. Bretz *et al.*, in *Plasma Physics and Controlled Nuclear Fusion Research* (International Atomic Energy Agency, Vienna, 1992), Vol. 1, p. 551.
[14] R. J. Hawryluk *et al.*, in *Plasma Physics and Controlled Nuclear Fusion Research 1986* (International Atomic Energy Agency, Vienna, 1987), Vol. 1, p. 51.
[15] F. Romanelli and F. Zonca, Phys. Fluids B **5**, 4081 (1993).
[16] J. W. Connor, J. B. Taylor, and H. R. Wilson, Phys. Rev. Lett. **70**, 1803 (1993).
[17] R. Benzi, S. Succi, and M. Vergassola, Phys. Rep. **222**, 145 (1992).
[18] H. Chen, S. Chen, and W. H. Matthaeus, Phys. Rev. A **45**, 5339 (1992).
[19] A. Bartoloni, C. Battista, S. Cabasino, P. S. Paolucci, J. Pech, R. Sarno, G. M. Todesco, M. Torelli, W. Tross, P. Vicini, R. Benzi, N. Cabibbo, F. Massaioli, and R. Tripiccione, Int. J. Mod. Phys. C **4**, 993 (1993).
[20] R. Tripiccione, Int. J. Mod. Phys. C **4**, 265 (1993).
[21] D. O. Martinez, S. Chen, and W. H. Matthaeus, Phys. Plasmas **1**, 1850 (1994).
[22] S. Tsai, F. W. Perkins, and T. H. Stix, Phys. Fluids **13**, 2108 (1970).
[23] F. L. Hinton and C. W. Horton, Phys. Fluids **14**, 116 (1971).
[24] S. Wolfram, J. Stat. Phys. **45**, 471 (1986).
[25] S. Chapman and T. G. Cowling, *Mathematical Theory of Non-uniform Gases* (Cambridge University Press, Cambridge, 1953).